



Hyperspectral Raman microscopy can accurately differentiate single cells of different human thyroid nodules

MARCOS A. S. DE OLIVEIRA,¹ MICHAEL CAMPBELL,² ALAA M. AFIFY,¹
ERIC C. HUANG,^{3,4} AND JAMES W. CHAN^{1,4,*}

¹Department of Pathology & Laboratory Medicine, Univ. of California Davis, Sacramento, CA 95817, USA

²Department of Surgery, Univ. of California Davis, Sacramento, CA 95817, USA

³Department of Pathology, Univ. of Washington, Seattle, WA 98104, USA

⁴ECH and JWC contributed equally as senior authors

*jwchan@ucdavis.edu

Abstract: We report on the use of line-scan hyperspectral Raman microscopy in combination with multivariate statistical analyses for identifying and classifying single cells isolated from clinical samples of human thyroid nodules based on their intrinsic Raman spectral signatures. A total of 248 hyperspectral Raman images of single cells from benign thyroid ($n = 127$) and classic variant of papillary carcinoma ($n = 121$) nodules were collected. Spectral differences attributed to phenylalanine, tryptophan, proteins, lipids, and nucleic acids were identified for benign and papillary carcinoma cells. Using principal component analysis and linear discriminant analysis, cells were identified with 97% diagnostic accuracy. In addition, preliminary data of cells from follicular adenoma ($n = 20$), follicular carcinoma ($n = 25$), and follicular variant of papillary carcinoma ($n = 18$) nodules suggest the feasibility of further discrimination of subtypes. Our findings indicate that hyperspectral Raman microscopy can potentially be developed into an objective approach for analyzing single cells from fine needle aspiration (FNA) biopsies to enable the minimally invasive diagnosis of “indeterminate” thyroid nodules and other challenging cases.

© 2019 Optical Society of America under the terms of the [OSA Open Access Publishing Agreement](#)

1. Introduction

Thyroid cancer is the most common endocrine malignancy and ninth most common overall cancer with an estimated 53,990 new cases in the United States in 2018 [1]. It is more prevalent in females, accounting for more than 75% of the cases. Thyroid cancer can occur in any age, but it is most common after age 30, with increasing aggressiveness in older patients [2]. The cornerstone for evaluating most thyroid nodules is a neck ultrasound followed by fine-needle aspiration (FNA) in sonographically suspicious nodules. Approximately 10-30% of thyroid nodules have “indeterminate” cytology according to the criteria set forth by the Bethesda System for Reporting Thyroid Cytopathology [3]. In these cases the cytopathologist cannot determine if the nodule is benign or malignant and the patient is faced with the uncertainty of whether the thyroid should be surgically removed. Recently, various genetic based molecular studies have been developed to aid clinicians in the management of patients with indeterminate thyroid nodules; but, the positive predictive value has been suboptimal [4]. As such, thyroidectomy remains the treatment of choice, although majority of the excised nodules are ultimately benign. Hence, a novel approach that can more accurately diagnose and differentiate thyroid nodules would avoid unnecessary surgeries and have a major impact in patient care and management.

Raman spectroscopy is a label-free spectroscopic technique based on inelastic scattering of light by vibrational modes of chemical bonds that allows for the identification of intrinsic molecules (e.g. protein, lipids, amino acids, nucleic acids) in cells and tissues. Subtle

differences in chemical composition and structure can lead to changes in peak intensities or positions in a Raman spectrum. Raman spectroscopy provides several advantages for cytopathology applications [5,6]. It can provide intrinsic chemical information of the sample without requiring exogenous labels or stains, has subcellular spatial resolution if implemented into a confocal microscope, and is nondestructive and noninvasive. Previous studies have demonstrated the use of Raman spectroscopy to improve the diagnosis of thyroid tissues [7–11]. Here, we extend this technology for diagnosing human thyroid cancers at the single cell level, with the goal of developing Raman spectroscopy as an ancillary spectral cytopathology tool to improve the accuracy of diagnosing thyroid nodules. In this study, we performed line-scan hyperspectral Raman microscopy on single cells isolated from benign and neoplastic human thyroid nodules from clinical samples and applied multivariate statistical methods, principal component analysis (PCA) and linear discriminant analysis (LDA), to analyze the multidimensional spectral data for the purposes of optimizing group separation and determining the diagnostic accuracy of the Raman spectral signatures in various thyroid nodules.

2. Materials and methods

2.1 Sample collection

This study is approved by our Institutional Review Board (UC Davis, Sacramento, CA). All patients were consented prior to study enrollment. Representative samples of the fresh nodules were collected for the study. Nodules that had insufficient residual tissue after diagnostic sampling were excluded from the study. The diagnostic materials were processed according to routine diagnostic surgical pathology with hematoxylin and eosin (H&E) stain, and the final diagnosis rendered is confirmed by a second pathologist for the study.

2.2 Sample preparation

Tissue samples were dissociated into single cells using established methods [12]. Briefly, the samples were incubated at 37°C in a collagenase (Worthington **Type 2**) solution 300U/ml in Hank's balanced salt solution (HBSS) for a few hours to digest the tissue. After digestion, single cells were isolated from larger pieces of tissue fragments by using a nylon mesh with 70µm pore size (Corning cell strainer). The isolated cells were washed a few times by centrifugation in HBSS, after which the supernatant was discarded and the packed cells resuspended for a few minutes into a 4% paraformaldehyde in phosphate buffered saline (PBS) solution for fixation. The fixed cells were then washed by centrifugation and the supernatant was re-suspended in PBS solution. The cell solution was pipetted onto a #1 thickness quartz coverslip that was mounted in a cell chamber holder (Thermo Fisher Scientific). Cells remained immersed in PBS solution for the duration of the Raman spectroscopy measurements.

2.3 Hyperspectral Raman microscopy

Hyperspectral Raman images of individual cells were acquired using a previously published method [13]. Briefly, a master oscillator power amplifier fiber laser system (Sacher-Laser) with a wavelength of 785 nm and a maximum power of 2 W is used as the excitation source. The laser beam passes a narrow 785 nm maxline laser-line clean-up filter (Semrock, LL01-785) to ensure monochromatic excitation and an achromatic cylindrical lens (Thorlabs, $f = 100$ mm) that focuses the Gaussian beam into a line profile. The cylindrical lens sits on a rotational mount for adjusting the orientation of the line to ensure that it is properly imaged onto the entrance slit of the spectrometer (PI Acton, SpectraPro SP2300i). After the cylindrical lens, the line-profile is imaged by an achromatic lens (Thorlabs, $f = 500$ mm) onto the back aperture of a 60x, 1.2 N.A. water immersion objective lens (Olympus, UPlanSApo) and focused into the sample plane. The length of the line at the sample plane is 50 µm with a

diffraction-limited width. The cell sample sits on a motorized flat top translational stage (ProScan Prior II) of an inverted microscope (Leica, DM IRM), allowing for scan. The Raman signals generated from the line shaped focal region are collected by the same objective lens and separated from the excitation source by a 785 nm dichroic long pass filter (Semrock, LP02-785RU). The Raman signals pass through another razoredge long pass filter (Semrock, LP02-785RE) and are imaged by an achromatic lens (Thorlabs, $f = 125$ mm), onto the entrance-slit of the spectrometer. The slit is adjusted to a width of 20 μm . A 600 grooves per mm grating is used to disperse the Raman signals from the line pattern, which is imaged onto a back-illuminated deep-depletion CCD detector (PI Acton, Pixis100). The image of the 50 μm long line is projected onto 100 pixels on the CCD chip, resulting in 0.5 μm per pixel. Typical Raman acquisition times per line is 50 seconds leading to a full hyperspectral Raman image of a single cell within minutes by scanning the cell with 1 μm step in the direction perpendicularly to the excitation laser line.

2.4 Data analysis

Background removal was first performed on the Raman spectra using a fully automated method for subtraction of fluorescence from biological Raman spectra [14]. Raman spectra were normalized with respect to the area under the curve. Multivariate statistical analysis was then performed on the multidimensional Raman spectral data for objective identification and classification of single thyroid cells. PCA is an unsupervised method that is used to identify the combination of Raman spectral features that maximize the data variance. These features are captured in a new set of variables called principal components (PCs) in a reduced dimension. The first few PCs typically account for the majority of the data variance. However, as an unsupervised method, PCA has no prior knowledge about the groupings of the spectral data, which means it is not suitable for the purposes of group separation. LDA is a supervised technique and is useful for discriminating between groups. So, for the purposes of optimizing group classification, a PCA-LDA model was developed in which PCs were used as the input variables for LDA. A 'leave-N-out' cross-validation technique was used to test the classification sensitivity and specificity of the PCA-LDA model. This procedure involves taking all K-N cells as a training set to build the LDA model, which is then used to classify the N 'blind' cells that were left out. This is done repeatedly for every possible group of N in the set of K cells. The accuracy of a prediction cross validation method of Raman spectra was presented by using the confusion matrix, where cells were classified as true negative (TN), false positive (FP), true positive (TP) and false negative (FN). Diagnostic accuracy, sensitivity and specificity were calculated. All homemade algorithms were written in Matlab (Mathworks, USA).

3. Results and discussion

Table 1 summarizes the patient sample characteristics used in this study. 228 cells from 10 different thyroid nodules (5 benign, 5 papillary carcinomas) underwent Raman spectroscopic analysis and hyperspectral Raman images were acquired from each individual cell.

Table 1. Clinical thyroid tissue samples

Specimen	Final Pathologic Diagnosis	# of Raman images
1	Benign nodular hyperplasia	28
2	Benign nodular hyperplasia	36
3	Benign nodular hyperplasia	20
4	Benign nodular hyperplasia	29
5	Benign nodular hyperplasia	14
6	Papillary carcinoma, classic variant	28
7	Papillary carcinoma, classic variant	29
8	Papillary carcinoma, classic variant	17
9	Papillary carcinoma, classic variant	16
10	Papillary carcinoma, classic variant	31
		Total:248

Figure 1 shows bright-field images of (a) classic variant of papillary thyroid carcinoma (CVPTC) and (g) benign single follicular cell. False color Raman images for the CVPTC (b-f) and benign (h-l) cell are generated using the band area intensities of select Raman peaks centered at 1003, 1080, 1293, 1430, and 1667 cm^{-1} . The bar scale was kept constant for all images. The sizes of the Raman images are typically 60x30 pixels. The Raman images in Fig. 1 indicate that there are several potential spectral differences between CVPTC and benign cells.

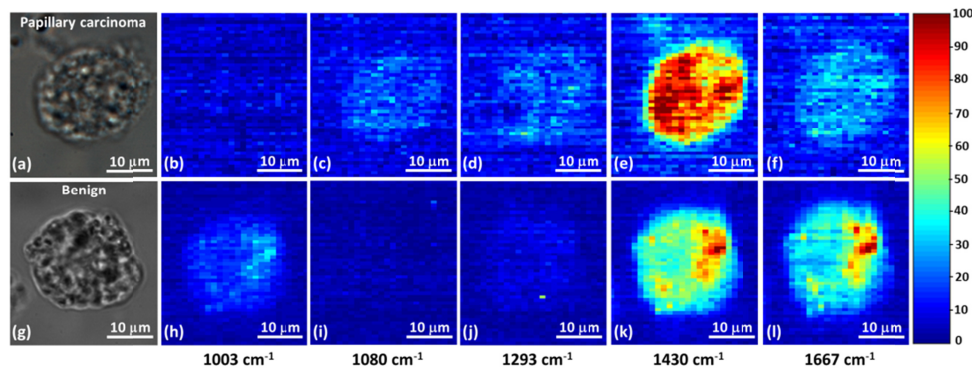


Fig. 1. Brightfield and Raman images of (a-f) papillary thyroid carcinoma cell and (g-l) benign follicular cell for select Raman bands.

To convert the hyperspectral Raman image of a cell into a single Raman spectrum that accurately represents the total chemical composition of the cell, we sum up the spectral signals from all pixels belonging to it in the Raman image. These single cell Raman spectra are used in all subsequent analysis for discriminating and classifying cell types. Figure 2 shows the average Raman spectra of 127 benign (blue line) and 121 CVPTC (red line) cells. The light gray shadows represent ± 1 standard deviations (SD) over the average values. The main spectral differences between benign and CVPTC cells, as emphasized in the difference spectrum in Fig. 2(c), are revealed in the 1003 cm^{-1} , 1031 cm^{-1} , 1080 cm^{-1} , 1205 cm^{-1} , 1260 cm^{-1} , 1293 cm^{-1} , 1362 cm^{-1} , 1430 cm^{-1} , 1667 cm^{-1} Raman band intensities. Table 2 shows the molecular assignment of these Raman peaks [7,9,11,15].

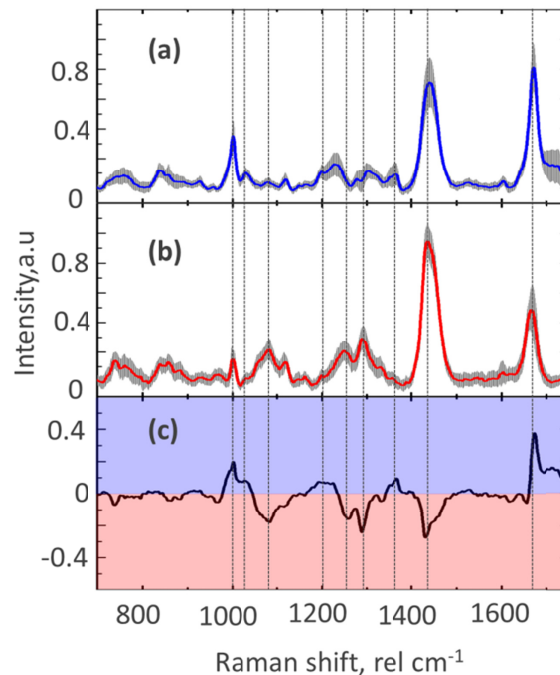


Fig. 2. Average Raman spectra of (a) 127 benign (blue line) and (b) 121 PTC classic variant (red line) cells. The gray shadows represent ± 1 standard deviations (SD) over the average values. (c) The difference spectrum (benign – CVPTC) highlights the peaks that are associated with benign cells (blue shade) and CVPTC cells (red shade).

Benign cells have higher peak intensities at 1003 cm^{-1} , 1031 cm^{-1} , 1205 cm^{-1} , 1362 cm^{-1} and 1667 cm^{-1} compared to malignant cells, suggesting that benign cells on average contain more phenylalanine, tryptophan, and protein. CVPTC cells exhibited higher peak intensities at 1080 cm^{-1} , which is assigned to phosphodiester groups in nucleic acids, and 1260 cm^{-1} , 1293 cm^{-1} and 1430 cm^{-1} , which are assigned to lipids. Most of the differences observed in our study agree with previous literature that also used Raman spectroscopy with 785 nm excitation to study thyroid tissues [10,11]. Neto et al. [11] have observed decreases in amide I protein and phenylalanine spectral peaks and increases in lipid peaks for papillary thyroid carcinoma. Li et al. [10] have observed decreases in phenylalanine peaks and increases in nucleic acid peaks for thyroid cancer tissues. Previous work [8,9], also using Raman spectroscopy to study thyroid tissues, reported differences in the carotenoid Raman bands for carcinoma and healthy thyroid tissues. These bands were observed mostly due to the resonance Raman effect by using a 532 nm excitation laser. However, these contributions were not observed in our Raman spectra because, with our 785 nm excitation source, we did not explore resonance effects in our study.

Additionally, Gniadecka et al. observed a reduction in amide I protein and phenylalanine peaks in Raman spectra for melanoma skin cancer [16]. Miyagi et al. have shown, through plasma free amino acid (PFAA) profiling, decreases in phenylalanine levels in patients with gastric cancer [17]. Previous works have also shown that tryptophan levels were reduced in esophageal cancer [18,19]. Jordan O'Malley et. al. [20] for example, by using Raman microspectroscopy, suggest lipids as a potential biomarker in prostate cancer due to lipids work as one of the major drivers for growth and membrane synthesis in malignant cells. Bergholt et al. [21], by using *in vivo* Raman endoscopy to study esophageal cancer, have found significant increases in nucleic acids for patients with cancer and suggest that may be a suitable biomarker to discriminate normal and cancer tissues.

Table 2. Raman band positions and assignments [7,9,11,15]. (Note: v: stretching vibration; vs: symmetrical stretching vibration; δ : bending vibration).

Band position (rel cm^{-1})	Raman band Assignments
1003	Phenylalanine vs(C-C); protein
1031	Phenylalanine (δ (C-H) and C-H in-plane bending); protein (C-N stretching); carbohydrate residues of collagen
1080	Phosphodiester groups in nucleic acids; v(C-C); vs(PO^{2-})
1205	Phenylalanine; tryptophan; adenine and tyrosine (ring breathing); amide III; v(C-C ₆ H ₅)
1260	Lipids
1293	Cytosine; lipid and collagen
1362	Tryptophan
1430	Lipid (CH ₂ scissoring and δ (CH ₃));
1667	Amide I (proteins); protein band carbonyl v(C=O); lipids v(C=O)

Figure 3(a) shows a 3D PCA scatter plot of the single cell Raman spectra based on the first three principal components (PCs), which account for 60% of the total variance in the Raman spectral data. Figure 3(b) shows the first three component coefficients, which highlight the combination of the Raman spectral features that contribute the most to maximizing the data variance. PC1, which captures the most variance, is similar to the difference spectrum in Fig. 2(c). The scatter plot shows that the first 3 PCs can separate the benign and CVPTC cells into distinct groups.

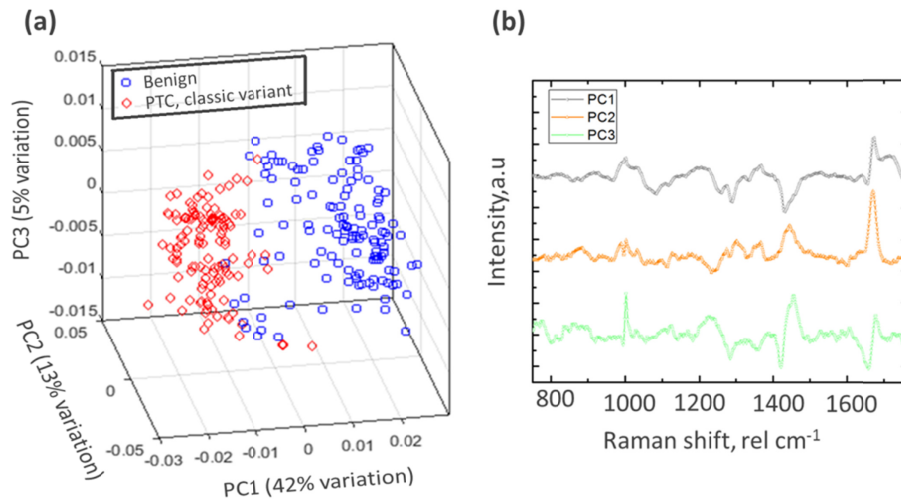


Fig. 3. (a) 3D PCA score plot of all individual Raman spectra for benign (blue circles) and CVPTC (red diamonds) cells. (b) Offset plot of the first three PCs coefficients.

PCA-LDA analysis was performed by using the first three PCs as the input variables for LDA. Figure 4 shows 2D (4a) and 3D (4b) PCA-LDA plots, with 95% interval confidence, covariance error ellipses and ellipsoids.

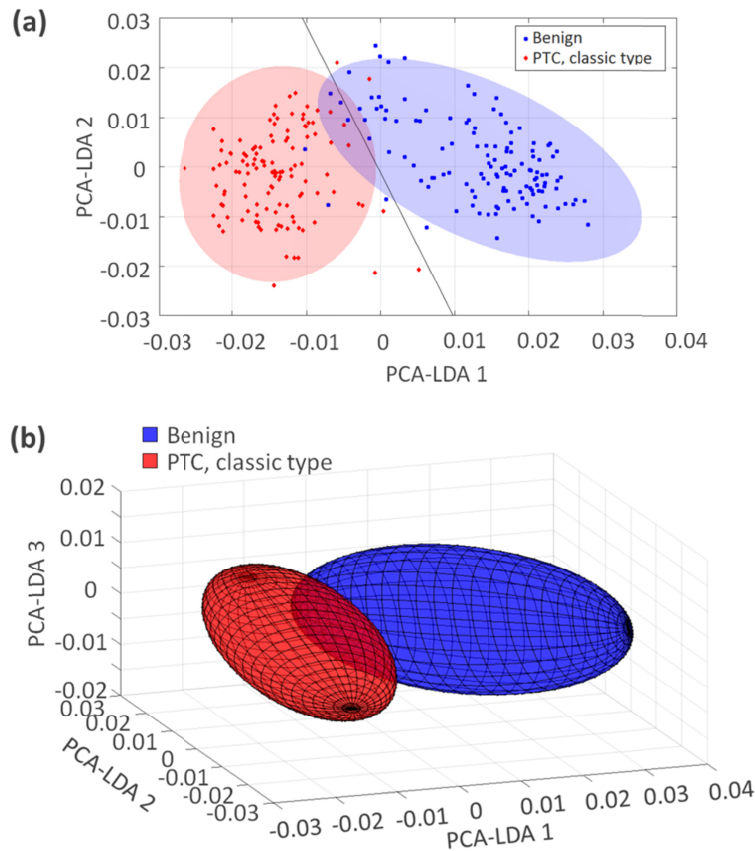


Fig. 4. (a) 2D and (b) 3D PCA-LDA score plots of benign (blue) and papillary carcinoma (red) cells with 95% interval confidence covariance error ellipses/ellipsoids.

Leave-N-out cross-validation was performed for classifying all 248 (K) cell spectra. A training set of 238 (K-N) cell spectra was used to classify the 10 (N) cell spectra that were left out of the training set by associating the N unknown spectra with the closest cluster in the training set. This process was repeated for all possible groups of N spectra in the set. The accuracy of the prediction method was quantified in the confusion matrix shown in Table 3. The cell misclassification may be due to cell-to-cell biological variability and/or PCA capturing only 60% of the data variance with the first 3 PCs.

Table 3. Confusion matrix of all representative Raman spectra for 127 benign and 121 papillary carcinoma cells.

Confusion Matrix		
Benign	123 (TN)	4 (FP)
CVPTC	2(FN)	119 (TP)

Diagnostic accuracy (DA) is a global measure used for general estimation of discriminative power, and is expressed as a proportion of correctly classified subjects (TP + TN) among all subjects. Sensitivity and specificity are also expressed as a percentage and defined by $TP/(TP + FN)$ and $TN/(TN + FP)$, respectively. In this analysis, the two groups (CVPTC vs. benign) of cells tested were correctly classified with 97% diagnostic accuracy, 98% sensitivity and 97% specificity.

In addition to showing the ability to accurately discriminate benign follicular cells from CVPTC, we present preliminary results suggesting that other cell subtypes can be discriminated from each other as well. The same methods presented in Section 2 were used. Figure 5 shows the average Raman spectra of 20 follicular thyroid adenoma (FTA), 25 follicular thyroid carcinoma (FTC) and 18 follicular variant of papillary thyroid carcinoma (FVPTC) cells. The light gray shadows represent ± 1 standard deviations (SD) over the average values.

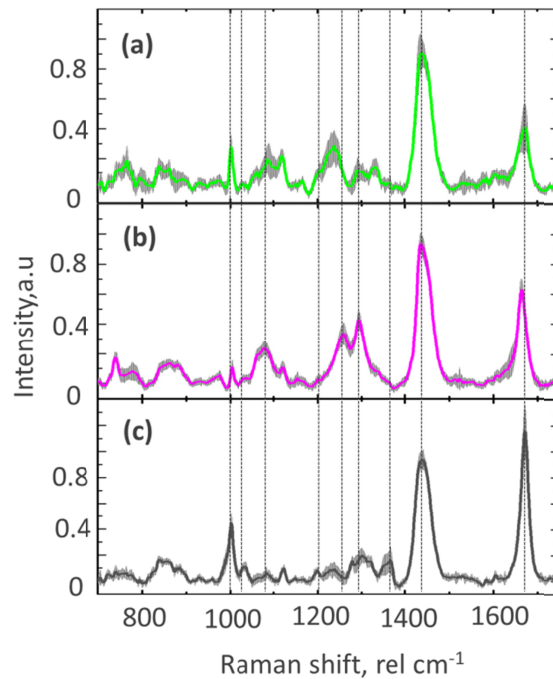


Fig. 5. Average Raman spectra of (a) 20 FTA (green line), (b) 20 FTC (magenta line) and (c) 18 FVPTC (dark gray line) cells. The light gray shadows represent ± 1 standard deviations (SD) over the average values.

Figure 6 shows 2-D and 3-D PCA-LDA plots comparing FTA ($n = 20$) with FTC ($n = 25$), and FVPTC ($n = 18$) with CVPTC ($n = 121$). The results of the leave-N-out validation approach, shown in the confusion matrices in Fig. 6, show 100% diagnostic accuracy, sensitivity, and specificity when comparing FTA and FTC, and 98%, 94%, and 98%, respectively, when comparing CVPTC and FVPTC. These results have potential clinical significance, because current FNA analysis, which is the cornerstone, minimally invasive method to exclude malignant thyroid nodules, cannot distinguish follicular adenoma from follicular carcinoma. As such, this leads to management conundrums for clinicians and, ultimately, a thyroidectomy is performed for a definitive diagnosis.

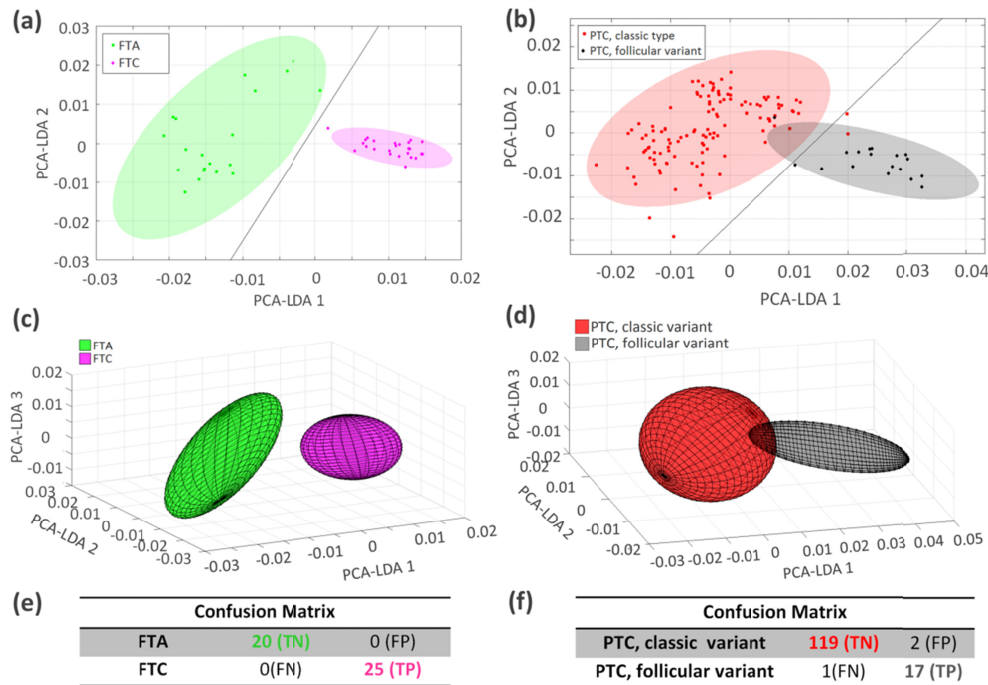


Fig. 6. (a)-(b) 2D and (c)-(d) 3D PCA-LDA score plot from 20 FTA (green plot), 25 FTC (magenta plot), 18 FVPTC (dark gray plot) and 121 CVPTC (red plot) cells. (e)-(f) Confusion matrices.

Table 4 summarizes the diagnostic accuracy, sensitivity, and specificity values for different pairings of cell type.

Table 4. Performance of the statistical (PCA-LDA with leave-N-out cross validation) analysis in discriminating thyroid cells.

Comparison	Sensitivity (%)	Specificity (%)	DA (%)
Benign vs. CVPTC	98	97	97
Benign vs. FTA	90	97	96
Benign vs. FTC	100	99	99
Benign vs. FVPTC	89	83	83
FTA vs. CVPTC	94	85	93
FTA vs. FTC	100	100	100
FTA vs. FVPTC	94	95	95
FTC vs. CVPTC	84	92	86
FTC vs. FVPTC	94	100	98
CVPTC vs. FVPTC	94	98	98

4. Conclusion

This study shows that line scan hyperspectral Raman microscopy, in combination with PCA-LDA analysis and classification is able to accurately differentiate cells from different types of thyroid nodules with high sensitivity and specificity. While other groups have used micro-Raman spectroscopy for the discrimination of thyroid commercial cell lines [15,22], our work to our knowledge is the first single cell Raman spectroscopy study on clinical patient specimens. Furthermore, our methodology of converting a hyperspectral image into a single cell Raman spectrum more accurately captures the chemical composition of the entire cell compared to other studies that acquire a Raman spectrum of a cell by sampling only an arbitrary fraction of the cell volume [23]. The high reproducibility and diagnostic accuracy of

our data may be attributed to our method's ability to adequately sample the entire cell. Our preliminary results even show excellent discrimination of cells that cannot be distinguished by current cytopathologic FNA analysis. Future studies will focus on FNA biopsy samples and will analyze other "indeterminate" thyroid nodules. We believe this novel approach can be developed into an objective and accurate ancillary tool for analyzing FNA samples to improve diagnostic cytopathology and avoid unwarranted surgeries.

Funding

Collaborative for Diagnostic Innovation Grant from the UC Davis Department of Pathology and Laboratory Medicine; UC Davis Academic Senate Grant.

Disclosures

The authors declare no conflicts of interest.

References

1. R. L. Siegel, K. D. Miller, and A. Jemal, "Cancer Statistics, 2018," *CA Cancer J. Clin.* **68**(1), 7–30 (2018).
2. N. Kwong, M. Medici, T. E. Angell, X. Liu, E. Marqusee, E. S. Cibas, J. F. Krane, J. A. Barletta, M. I. Kim, P. R. Larsen, and E. K. Alexander, "The Influence of Patient Age on Thyroid Nodule Formation, Multinodularity, and Thyroid Cancer Risk," *J. Clin. Endocrinol. Metab.* **100**(12), 4434–4440 (2015).
3. E. S. Cibas and S. Z. Ali, "The 2017 Bethesda System for Reporting Thyroid Cytopathology," *Thyroid* **27**(11), 1341–1346 (2017).
4. R. L. Ferris, Z. Baloch, V. Bernet, A. Chen, T. J. Fahey 3rd, I. Ganly, S. P. Hodak, E. Kebebew, K. N. Patel, A. Shaha, D. L. Steward, R. P. Tufano, S. M. Wiseman, and S. E. Carty, "American Thyroid Association Statement on Surgical Application of Molecular Profiling for Thyroid Nodules: Current Impact on Perioperative Decision Making," *Thyroid* **25**(7), 760–768 (2015).
5. A. T. Harris, A. Rennie, H. Waqar-Uddin, S. R. Wheatley, S. K. Ghosh, D. P. Martin-Hirsch, S. E. Fisher, A. S. High, J. Kirkham, and T. Upile, "Raman spectroscopy in head and neck cancer," *Head Neck Oncol.* **2**(1), 26 (2010).
6. T. Huser and J. Chan, "Raman spectroscopy for physiological investigations of tissues and cells," *Adv. Drug Deliv. Rev.* **89**, 57–70 (2015).
7. C. S. B. Teixeira, R. A. Bitar, H. S. Martinho, A. B. O. Santos, M. A. V. Kulcsar, C. U. M. Friguglietti, R. B. da Costa, E. A. L. Arisawa, and A. A. Martin, "Thyroid tissue analysis through Raman spectroscopy," *Analyst (Lond.)* **134**(11), 2361–2370 (2009).
8. J. V. Rau, M. Fosca, V. Graziani, C. Taffon, M. Rocchia, M. Caricato, P. Pozzilli, A. Onetti Muda, and A. Crescenzi, "Proof-of-concept Raman spectroscopy study aimed to differentiate thyroid follicular patterned lesions," *Sci. Rep.* **7**(1), 14970 (2017).
9. J. V. Rau, V. Graziani, M. Fosca, C. Taffon, M. Rocchia, P. Crucitti, P. Pozzilli, A. Onetti Muda, M. Caricato, and A. Crescenzi, "RAMAN spectroscopy imaging improves the diagnosis of papillary thyroid carcinoma," *Sci. Rep.* **6**(1), 35117 (2016).
10. Z. F. Li, C. Li, D. Lin, Z. F. Huang, J. J. Pan, G. N. Chen, J. Q. Lin, N. R. Liu, Y. Yu, S. Y. Feng, and R. Chen, "Surface-enhanced Raman spectroscopy for differentiation between benign and malignant thyroid tissues," *Laser Phys. Lett.* **11**(4), 045602 (2014).
11. L. P. Medeiros Neto, L. F. das Chagas E Silva de Carvalho, L. D. Santos, C. A. Tellez Soto, R. de Azevedo Canevari, A. B. de Oliveira Santos, E. S. Mello, M. A. Pereira, C. R. Cernea, L. G. Brandão, and A. A. Martin, "Micro-Raman spectroscopic study of thyroid tissues," *Photodiagn. Photodyn. Ther.* **17**, 164–172 (2017).
12. R. C. Miller, T. Hiraoka, N. Nakamura, H. Tenou, K. J. Kopecky, M. P. Jones, and M. N. Gould, "In vitro culture of human thyroid cells; methods and application to radiation biology," *J. Radiat. Res. (Tokyo)* **26**(3), 269–282 (1985).
13. I. W. Schie, L. Alber, A. L. Gryshuk, and J. W. Chan, "Investigating drug induced changes in single, living lymphocytes based on Raman micro-spectroscopy," *Analyst (Lond.)* **139**(11), 2726–2733 (2014).
14. C. A. Lieber and A. Mahadevan-Jansen, "Automated method for subtraction of fluorescence from biological Raman spectra," *Appl. Spectrosc.* **57**(11), 1363–1367 (2003).
15. D. O'Dea, M. Bongiovanni, G. P. Sykietis, P. G. Ziros, A. D. Meade, F. M. Lyng, and A. Malkin, "Raman spectroscopy for the preoperative diagnosis of thyroid cancer and its subtypes: An in vitro proof-of-concept study," *Cytopathology* **30**(1), 51–60 (2019).
16. M. Gniadecka, P. A. Philipsen, S. Sigurdsson, S. Wessel, O. F. Nielsen, D. H. Christensen, J. Hercogova, K. Rossen, H. K. Thomsen, R. Gniadecki, L. K. Hansen, and H. C. Wulf, "Melanoma diagnosis by Raman spectroscopy and neural networks: structure alterations in proteins and lipids in intact cancer tissue," *J. Invest. Dermatol.* **122**(2), 443–449 (2004).
17. Y. Miyagi, M. Higashiyama, A. Gochi, M. Akaike, T. Ishikawa, T. Miura, N. Saruki, E. Bando, H. Kimura, F. Imamura, M. Moriyama, I. Ikeda, A. Chiba, F. Oshita, A. Imaizumi, H. Yamamoto, H. Miyano, K. Horimoto, O.

- Tochikubo, T. Mitsushima, M. Yamakado, and N. Okamoto, "Plasma Free Amino Acid Profiling of Five Types of Cancer Patients and Its Application for Early Detection," *PLoS One* **6**(9), e24143 (2011).
18. X. Zhang, L. Xu, J. Shen, B. Cao, T. Cheng, T. Zhao, X. Liu, and H. Zhang, "Metabolic signatures of esophageal cancer: NMR-based metabolomics and UHPLC-based focused metabolomics of blood serum," *Biochim. Biophys. Acta* **1832**(8), 1207–1216 (2013).
 19. J. Zhang, J. Bowers, L. Liu, S. Wei, G. A. N. Gowda, Z. Hammoud, and D. Raftery, "Esophageal Cancer Metabolite Biomarkers Detected by LC-MS and NMR Methods," *PLoS One* **7**(1), e30181 (2012).
 20. J. O'Malley, R. Kumar, A. N. Kuzmin, A. Pliss, N. Yadav, S. Balachandar, J. Wang, K. Attwood, P. N. Prasad, and D. Chandra, "Lipid quantification by Raman microspectroscopy as a potential biomarker in prostate cancer," *Cancer Lett.* **397**, 52–60 (2017).
 21. M. S. Bergholt, W. Zheng, K. Lin, K. Y. Ho, M. Teh, K. G. Yeoh, J. B. Y. So, and Z. Huang, "In Vivo Diagnosis of Esophageal Cancer Using Image-Guided Raman Endoscopy and Biomolecular Modeling," *Technol. Cancer Res. Treat.* **10**(2), 103–112 (2011).
 22. A. T. Harris, M. Garg, X. B. B. Yang, S. E. Fisher, J. Kirkham, D. A. Smith, D. P. Martin-Hirsch, and A. S. High, "Raman spectroscopy and advanced mathematical modelling in the discrimination of human thyroid cell lines," *Head Neck Oncol.* **1**(1), 38 (2009).
 23. I. W. Schie and J. W. Chan, "Estimation of spectra sample size for characterizing single cells using micro-Raman spectroscopy," *J. Raman Spectrosc.* **47**(4), 384–390 (2016).